INTERNATIONAL JOURNAL FOR NUMERICAL METHODS IN FLUIDS
Int. J. Numer. Meth. Fluids 2003; **43**:1257–1277 (DOI: 10.1002/fld.506)

Non-linear time-domain models for irregular wave diffraction about offshore structures

Pierre Ferrant*,†, David Le Touzé and Karine Pelletier

Laboratoire de Mécanique des Fluides, Division Hydrodynamique Navale, CNRS UMR6598 École Centrale de Nantes, France

SUMMARY

This paper is devoted to the numerical simulation of non-linear wave diffraction by three-dimensional (3D) surface-piercing structures in the time domain. Two different methods are presented. First a second-order diffraction model is described, in which a boundary-element method combined with a time-stepping procedure are used to solve the first- and second-order diffraction problems in the time domain. The Stokes expansion approach of the free surface non-linearities results in relatively moderate simulation times, so that long simulations in irregular incident waves become feasible. The model has previously been systematically validated by comparison with available semi-analytical frequency domain results on regular wave diffraction about simplified geometries. In the present paper, the flexibility and stability of the time-domain approach to second-order wave diffraction are further demonstrated by the simulation of bichromatic wave diffraction over a large number of incident wave periods. The second part of the paper addresses the problem of fully non-linear wave diffraction. Again, the solution procedure is based on a boundary element method (BEM) solution of the boundary-value problem in the time domain, but the non-linear boundary conditions are accounted for without any approximation this time. In this fully non-linear diffraction model, an explicit description of the incident wave is exploited to solve the problem for the diffracted flow only. This approach has a number of practical advantages in terms of accuracy and computational efficiency. In previous publications related to this approach stream-function theory was utilized to model non-linear regular incident waves. In this paper, irregular two-dimensional (2D) incident waves are modelled by means of a recently developed fully non-linear time-domain pseudospectral formulation. An original coupling of this 2D pseudospectral model with the 3D non-linear BEM model is proposed, and its effectiveness is shown on the case of 2D wave packets interacting with a vertical bottom-mounted cylinder. Copyright © 2003 John Wiley & Sons, Ltd.

KEY WORDS: wave diffraction; potential flow; free surface; pseudospectral method; BEM; time domain

1. INTRODUCTION

The accurate estimation of hydrodynamic interaction effects represents a major concern in the design and operation of large offshore structures. Significant effects observed both at sea and at

* Correspondence to: P. Ferrant, Laboratoire de Mécanique des Fluides, Ecole Centrale de Nantes, 1 rue de la Noe, B.P. 92101, 44321 Nantes Cedex 3, France.
† E-mail: pierre.ferrant@ec-nantes.fr

Received 17 April 2002
Revised 15 November 2002

model scale, such as the 'springing' and 'ringing' behaviours of Tension Leg Platforms, cannot be described by the usual radiation–diffraction theory. Motivated by these problems, strong efforts have been devoted to the development of non-linear wave–body interaction theories. When flow separation is not significant, that is when the body is considered as 'large', the fluid problem can be formulated using potential flow theory. Two different approaches may then be adopted to cope with free surface non-linearities.

The first one is based on the assumption of weak non-linearity, so that all physical quantities can be developed as perturbation series with respect to a small parameter ε related to the wave steepness. Historically, second-order wave–body interaction problems have first been formulated and solved in the frequency domain, see e.g. References [1, 2]. In such formulations one is faced, at first order, with one independent problem for each of the frequencies of the incoming wave system, while at second-order independent problems are related to each sum and difference frequencies. More recently, time-domain solution methods for second-order diffraction problems have proved to represent a valuable alternative, Kim *et al.* [3], with a number of potential advantages. As an example, there is a great flexibility in the implementation of different free surface conditions, so that the inclusion of a current superimposed to second-order waves is possible without major difficulties, see Büchmann *et al.* [4]. Initially restricted to simplified problems such as vertical cylinders in regular waves, the time-domain approach has further been applied to more complex structures, by implementing higher-order local interpolation scheme for the computation of forcing terms on arbitrary free surface configurations, while extensive validation with respect to existing frequency domain benchmark results were produced [5].

The alternative consists in solving, in space and time, the complete non-linear boundary-value problem. In the most common approach in this spirit, the generation of waves by a wavemaker, their propagation and their interaction with the body are simulated as a single process. Within such a procedure it is possible to simulate the conditions of real physical experiments; however, numerical models developed in this way require considerable CPU and memory resources for obtaining reasonably accurate results in three dimensions [6]. Ferrant [7] proposed a fully non-linear diffraction formulation in which incident waves are described explicitly and a boundary-value problem is formulated for the diffracted quantities, without restriction on non-linearities. This non-linear diffraction approach proved to be computationally very efficient. Using stream-function theory [8] as an explicit model for non-linear regular waves, a parametric study of the non-linear influence of wave amplitude on higher harmonic diffraction loads was produced, while results of asymptotic second- and third-order theories were recovered at low amplitudes, see e.g. Reference [9]. Fully non-linear wave–current–body interaction problems were also solved using this scheme [10], with careful cross-validation with finite-order calculation [11].

In this paper, we present recent developments of both second-order and fully non-linear time-domain approaches of the diffraction problem. The second-order model, previously validated on regular waves, is being extended to irregular wave diffraction. The overall accuracy and stability of the scheme is illustrated by long simulations of the diffraction of bichromatic waves about vertical bottom mounted or truncated cylinders. This demonstration opens the way to long-term estimation of second-order wave–body interactions in irregular short-crested seas, a problem which will be addressed in future publications. Regarding fully non-linear diffraction, an extension of the scheme to irregular wave diffraction is proposed by representing incident waves using a pseudospectral 2D model. The successful coupling of this

2D pseudospectral model with the 3D BEM solver is illustrated by simulating the non-linear diffraction of 2D wave packets about a vertical bottom-mounted cylinder.

2. SECOND-ORDER TIME-DOMAIN MODELLING

In this section, we present the essential features, as well as recent results, of our second-order time-domain diffraction model. This scheme has been previously validated for regular Stokes waves diffraction, with emphasis placed on validation with respect to semi-analytical frequency domain benchmark results [5]. Developments are now focused on the extension to the simulation of irregular incoming waves. Within this progression, second-order diffraction of bichromatic waves, whose numerical results of interaction with surface-piercing cylinders are described hereafter, constitutes an intermediate step.

2.1. Mathematical formulation

We consider a three-dimensional fluid domain D, bounded by a free surface S_F, a body surface S_B and a flat bottom surface S_{BT} located at $(z=-h)$. The domain is of infinite extent in the horizontal directions, and a Cartesian fixed co-ordinate system $(O;\mathbf{x},\mathbf{y},\mathbf{z})$ is defined; z is positive upwards and O chosen at the centre of the body at the mean water level. Moreover, non-dimensional quantities are assumed in all the expressions of the present paper, based on a reference length L and with the acceleration of gravity g as the acceleration of reference. In a classical manner in the field of water waves, we chose the water depth h for reference length.

Then we place ourselves in the framework of potential flow theory, so that the governing equation for the velocity potential $\phi(x,y,z,t)$ in the fluid domain D is Laplace's equation

$$\Delta\phi(\mathbf{M})=0, \quad \mathbf{M}(x,y,z,t)\in D \tag{1}$$

Under the weak non-linearity assumption, the velocity potential ϕ and the free surface elevation η are expanded into perturbation series

$$\phi=\varepsilon\phi^{(1)}+\varepsilon^2\phi^{(2)}+O(\varepsilon^3) \tag{2}$$

$$\eta=\varepsilon\eta^{(1)}+\varepsilon^2\eta^{(2)}+O(\varepsilon^3) \tag{3}$$

where ε is a small parameter related to wave steepness $2A/\lambda$ (A being the wave amplitude and λ the wavelength).

After separation of the incident and scattered parts of each variable $\phi=\phi_i+\phi_d$ and $\eta=\eta_i+\eta_d$, these quantities are plugged into the free surface dynamic and kinematic conditions in order to formulate the boundary-value problems for the diffracted wave field at first and second orders ($k=1,2$, respectively)

$$\frac{\partial\phi_d^{(k)}}{\partial t}=-\eta_d^{(k)}-\eta_i^{(k)}-\frac{\partial\phi_i^{(k)}}{\partial t}+F_2^{(k)}-\nu(R)\phi_d^{(k)}, \quad \mathbf{M}(x,y,0,t)\in S_F \tag{4}$$

$$\frac{\partial\eta_d^{(k)}}{\partial t}=\frac{\partial\phi_d^{(k)}}{\partial z}+\frac{\partial\phi_i^{(k)}}{\partial z}-\frac{\partial\eta_i^{(k)}}{\partial t}+F_1^{(k)}-\nu(R)\eta_d^{(k)}, \quad \mathbf{M}(x,y,0,t)\in S_F \tag{5}$$

with first- and second-order forcing terms defined as

$$F_1^{(1)} = F_2^{(1)} = 0 \tag{6}$$

$$F_1^{(2)} = -\frac{\partial \phi^{(1)}}{\partial x}\frac{\partial \eta^{(1)}}{\partial x} - \frac{\partial \phi^{(1)}}{\partial y}\frac{\partial \eta^{(1)}}{\partial y} + \eta^{(1)}\frac{\partial^2 \phi^{(1)}}{\partial z^2} \tag{7}$$

$$F_2^{(2)} = -\frac{1}{2}|\nabla \phi^{(1)}|^2 - \eta^{(1)}\frac{\partial^2 \phi^{(1)}}{\partial z \partial t} \tag{8}$$

In order to avoid reflection of diffracted waves on the outer boundary of the domain, absorbing terms governed by the space function $\nu(R)$ have been added to the forcing terms in (4) and (5), where R is the horizontal distance to the centre of the body C_B. The extent of this absorbing zone, active from a distance R_{abs} to the outer boundary located at a distance R_{S_F} from C_B, is typically of the order of magnitude of the incident wavelength. In our calculations $\nu(R)$ is chosen as such

$$\nu(R) = 0 \quad \text{for } R < R_{abs} \tag{9}$$

$$\nu(R) = \frac{1}{2}\left(\frac{R - R_{abs}}{R_{S_F} - R_{abs}}\right)^2 \quad \text{for } R_{abs} < R < R_{S_F} \tag{10}$$

On the body, a no-flux Neumann condition applies

$$\frac{\partial \phi_d^{(k)}}{\partial n} = -\alpha(t)\frac{\partial \phi_i^{(k)}}{\partial n}, \quad \mathbf{M}(x, y, z, t) \in S_B \tag{11}$$

where $\alpha(t)$ is a temporal ramp function varying from 0 to 1 at start of the simulation, which is typically defined as one period of the first-order incident wave. This gradual imposition of the body condition for the diffracted potential avoids any possible shock at the beginning of the simulation.

Eventually, the condition on the sea bottom is

$$\frac{\partial \phi_d^{(k)}}{\partial n} = 0, \quad \mathbf{M}(x, y, z, t) \in S_{BT} \tag{12}$$

To supplement these equations, an extinction condition of the scattered potential at infinity, and an initial undisturbed incident wave condition must be added

$$\phi_d^{(k)} = 0 \quad k = 1, 2, \quad \mathbf{M}(x, y, z, 0) \in D \tag{13}$$

$$\phi_d^{(k)} \to 0 \quad k = 1, 2, \quad \mathbf{M}(x, y, z, t) \in D \quad (x, y) \to \infty \tag{14}$$

For the incoming wave field, an irregular wave pattern composed of n different frequencies $\omega_{j(j=1,n)}$ is used. The first-order solution can then be written as a simple superposition of n

first-order Airy waves

$$\eta_i^{(1)} = \sum_{j=1}^{n} A_j \cos(\omega_j t - k_j x) \tag{15}$$

$$\phi_i^{(1)} = \sum_{j=1}^{n} A_j \frac{\omega_j}{k_j} \frac{\cosh k_j(z+1)}{\sinh k_j} \sin(\omega_j t - k_j x) \tag{16}$$

where A_j is the amplitude of the jth component and k_j its wave number.

The second-order wave expression comes, on one hand, from the self-interaction of waves, and on the other hand, from the interaction of waves with each other. The resulting expressions for the second-order free-surface elevation and potential can then be split into two components, in order to point out the sum-frequency and difference-frequency modes. As an example, the formulations of solutions in the case of finite depth second-order wave–wave interaction can be found in Reference [12]. As well, the following expressions, expressed at $\mathbf{M}(x, y, z, t)$ in D, correspond to the second-order potential in the case of multichromatic incident waves propagating in the (O,x) direction:

$$\phi_i^{(2)} = \phi_i^{(2)+} + \phi_i^{(2)-} \tag{17}$$

$$\phi_i^{(2)\pm} = \sum_{j=1}^{n} \sum_{l=1}^{n} \frac{1}{2} \frac{a_{jl}^{\pm}}{((\omega_j \pm \omega_l)^2 - k^{\pm} \tanh k^{\pm})} \frac{\cosh k^{\pm}(z+1)}{\cosh k^{\pm}} \sin(\psi_j \pm \psi_l) \tag{18}$$

in which $\psi_j = k_j x - \omega_j t$, and where

$$a_{jl}^{\pm} = a_j a_l \left[\frac{1}{2} \left(\frac{\omega_j^3}{\sinh^2 k_j} \pm \frac{\omega_l^3}{\sinh^2 k_l} \right) + \omega_j \omega_l (\omega_j \pm \omega_l) \left(\frac{1}{\tanh k_j \tanh k_l} \mp 1 \right) \right] \tag{19}$$

$$k^{\pm} = \sqrt{k_j^2 + k_l^2 \pm 2k_j k_l} \tag{20}$$

The second-order free-surface elevation formulation is developed in the same way. Moreover, a time-dependent term $\delta(t)$ is added to the expression of the second-order potential to assure zero mean water elevation in time

$$\delta^2(t) = -\sum_{j=1}^{n} \frac{a_j^2 k_j t}{2 \sinh\ (2k_j)} \tag{21}$$

2.2. Numerical method

The boundary integral equation method is used to solve the first- and second-order boundary-value problems. Green's identity is applied to the scattered velocity potential and to the free space Green function ($G(M,M') = -1/4\pi MM'$, Rankine source); this leads to the following integral formulation of the problem:

$$\frac{\Omega(\mathbf{M})}{4\pi} \phi_d^{(k)}(\mathbf{M}) = \int_{S_{\mathbf{M}'}} \left[\phi_d^{(k)}(\mathbf{M}') \frac{\partial G}{\partial n'} - G \frac{\partial \phi_d^{(k)}}{\partial n'}(\mathbf{M}') \right] \mathrm{d}S_{\mathbf{M}'} \tag{22}$$

where $\Omega(\mathbf{M})$ stands for the internal solid angle at the considered point $\mathbf{M}(x, y, z, t)$, and $\mathbf{M}'$ is the integration point on the boundary of the fluid domain.

The boundary-value problem is solved by means of a BEM based on isoparametric triangular elements. The variation of the solution is taken linear over each element. In a second-order simulation the geometry of the domain is invariant in time, thus the kernel matrix of influence coefficients is calculated only once at the beginning of the simulation. The time integration of dynamic (4) and kinematic (5) free surface conditions is carried out through a fourth-order Runge–Kutta time-marching scheme.

The numerical calculation of the forcing terms requires the determination of the space derivatives of ϕ and η, at the nodes of the discretized domain. Therefore, the reliability of the solution directly depends on the accuracy of the numerical scheme used to evaluate these space derivatives. In order to extend the domain of application to arbitrary geometries, we have hence chosen local higher-order interpolation schemes based on local spline patches [13] allowing an arbitrary distribution of the mesh nodes. Depending on the location of the considered node on the free surface, pseudopolynomial splines or 'thin-plate' splines have been implemented to cope with the calculation of the space derivatives. These methods have previously been validated [5] for the calculation of the velocity potential derivatives in the cases of single or multiple cylinders, by comparison with semi-analytical solutions [14, 15].

2.3. *Results*

In order to check the effectiveness of our time-domain second-order diffraction model, it has first been validated with existing frequency domain reference results, in the case of single or multiple cylinders. An example of such a validation test on regular wave diffraction is briefly presented here. We consider a configuration of four cylinders placed at the corners of a square of side length d; so these cylinders of radius $a/h = \frac{1}{3}$ are equally spaced ($d/h = 2$). The wave number of the regular incoming wave field is $k_0 h = 1.036$, the domain discretized is cylindrical with $R_{S_F} = 14$ from the centre of the square. An absorbing zone is active from $R_{\text{abs}} = 7.5$ to R_{S_F}. Figure 1 shows the second-order maximum runup observed on the downwave cylinder, with A the wave amplitude. Our time-domain results are confronted to results issued from a frequency domain formulation (personal communication of Š. Malenica). The observed agreement is very satisfactory since the comparison on the second-order oscillatory runup is the most selective test for a second-order diffraction calculation.

We have then proceeded to calculations of irregular wave diffraction cases, described hereafter. The incoming wave field is composed of two different waves propagating along the (O, x) axis. Owing to the xOz symmetry plane the discretized domain is taken as half the physical domain. To simulate bichromatic waves diffraction, the mesh close to the cylinder has to be fine enough to resolve the smallest diffracted waves, and at the same time the domain has to be large enough for the longest waves to be correctly absorbed in the far field. For instance, in the present simulations the mesh density in the vicinity of the body is about 140 panels per smaller first-order wavelength, while the whole mesh counts 14 000 panels. The time step selected is about one 100th of the shorter first-order wave period.

First a bottom-mounted single circular cylinder is considered, with radius $a/h = 1/4$; the non-dimensional wave frequencies are $\omega_1 = 2.19$ and $\omega_2 = 2.68$, and their corresponding amplitudes $A_1/h = A_2/h = 0.0625$. The absorbing zone is active from $R_{\text{abs}} = 8$ to $R_{S_F} = 17$. Presented in Figure 2, the time series of first- and second-order runups on the cylinder cover

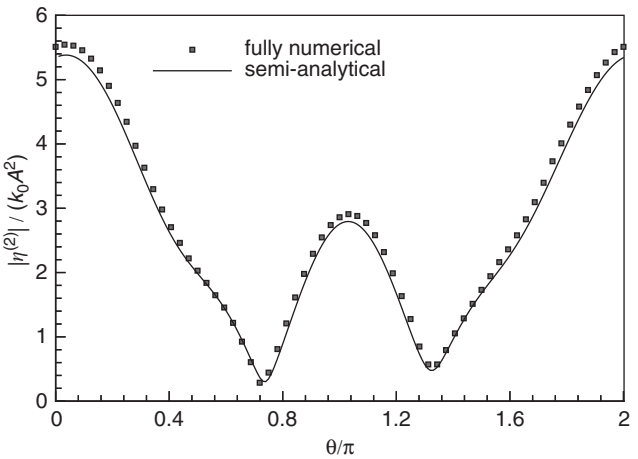

Figure 1. Second-order maximum runup on the downwave cylinder, $a/h = 0.25$, $d/h = 2$, $k_0 h = 1.036$.

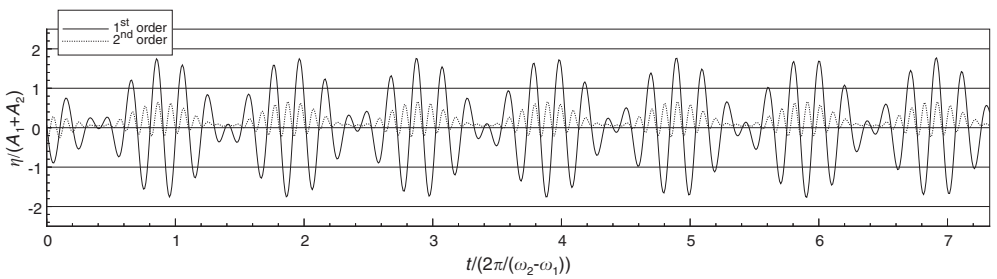

Figure 2. First- and second-order runups on the cylinder for $a/h = 0.25$, $\omega_1 = 2.19$ and $\omega_2 = 2.68$.

about seven second-order difference-frequency periods; the signals present a good stability. One finds another illustration of that case in Figure 3 where a snapshot of the free surface deformation is plotted, at an instant of maximum elevation at the upwave part of the cylinder. The incident 2D propagating and the scattered, radially expanding, wave fields are clearly observable.

In the second simulation, we chose one of the test cases recently proposed in the frame of ISSC'2000 [16]: a truncated vertical cylinder of radius $a = 8$ m, and draught $d = 24$ m is placed in water of depth $h = 489$ m. The characteristics of the bichromatic incident waves are $T_1 = 9$ s, $A_1 = 3.95$ m and $T_2 = 12$ s, $A_2 = 7.025$ m. The simulation has been run over approximately 10 periods of the difference-frequency second-order component, which corresponds to about 350 s real time. Figure 4 shows the different components of the runup. The perfect stability of the scattered part during the whole simulation is noticeable, which is especially visible in Figure 4(a). This is a reliable indication of the efficiency of the absorbing zone, since no visible perturbation is reflected back from the outer boundary. Time series of the total first- and second-order runups (incident + scattered) are plotted in Figure 4(b).

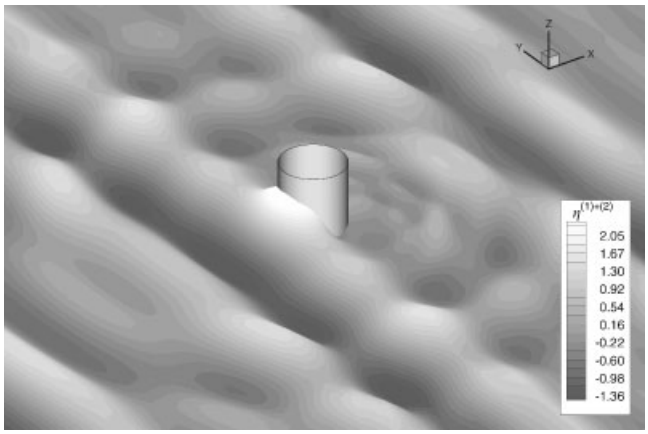

Figure 3. Instantaneous free surface elevation, $a/h = 0.25$, $\omega_1 = 2.19$ and $\omega_2 = 2.68$.

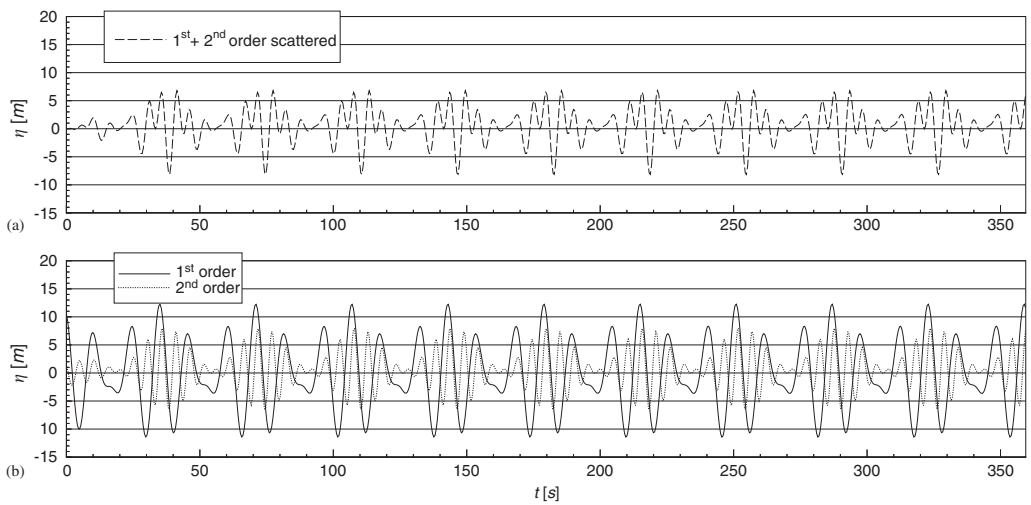

Figure 4. Runups of ISSC case: (a) total scattered runup, (b) first- and second-order runups (incident + scattered).

2.4. Comments

The second-order diffraction of bichromatic waves by truncated and bottom-mounted cylinders has been simulated over significant periods of time, demonstrating the stability and accuracy of our time-domain second-order diffraction model. A precise comparison with available frequency domain results for irregular incoming wave pattern is difficult, since our scheme delivers the total diffracted quantities, while frequency domain formulations give results independently for each frequency. However, the excellent validation results already obtained in regular waves give us a strong confidence in the bichromatic wave diffraction simulations presented in this paper. Second-order diffraction simulations in realistic short-crested seas will

be presented soon. In parallel, the implementation of an active absorption scheme combined with the absorbing layer is in progress, expected to lead to a reduction of the domain size and thus to further reduce memory and CPU requirements.

3. FULLY NON-LINEAR DIFFRACTION MODEL

In this section, a brief outline of the formulation of our 3D BEM fully non-linear diffraction model is given. More details on the implementation of this model, as well as extensive results in the case of regular wave diffraction with or without current were previously reported, see e.g. References [9–11].

3.1. Semi-Lagrangian formulation

As for the second-order model, we consider a three-dimensional fluid domain D, bounded by a free surface S_F, body surface S_B and bottom surface S_{BT} at $z=-h$, and of infinite extent in the horizontal directions. We remain in the frame of potential flow theory and as in Section 2 all the expressions are non-dimensionalized with respect to water depth h and the acceleration of gravity g. The fluid velocity inside the domain thus derives from a scalar potential satisfying Laplace's equation

$$\mathbf{V}(\mathbf{M}) = \nabla\phi(\mathbf{M}), \quad \mathbf{M}(x,y,z,t) \in D \tag{23}$$

$$\Delta\phi(\mathbf{M}) = 0, \quad \mathbf{M}(x,y,z,t) \in D \tag{24}$$

On the free surface, both kinematic and dynamic conditions must be satisfied. The kinematic condition states that the mass flux through the free surface is zero, and writes, in Lagrangian form

$$\frac{\mathrm{D}\mathbf{M}}{\mathrm{D}t} = \nabla\phi, \quad \mathbf{M}(x,y,z,t) \in S_F \tag{25}$$

If surface tension is ignored, the dynamic condition expresses the continuity of the pressure across the free surface, and derives from Bernoulli's equation

$$\frac{\mathrm{D}\phi}{\mathrm{D}t}(\mathbf{M}) = -z + \frac{1}{2}|\nabla\phi|^2, \quad \mathbf{M}(x,y,z,t) \in S_F \tag{26}$$

where $\mathrm{D}/\mathrm{D}t$ stands for the material derivative. Equations (25) and (26) suppose a fully Lagrangian description of the free surface, with markers identified as material points. In the present paper, the formulation will be modified by inhibiting the horizontal motions of free surface markers, leading to a semi-Lagrangian description. In such a formulation, the free surface vertical co-ordinate becomes implicitly single valued

$$z = \eta(x,y,t), \quad \mathbf{M}(x,y,z,t) \in S_F \tag{27}$$

Plugging this notation into (25) and (26), and after some manipulations, we obtain new forms of the non-linear kinematic and dynamic boundary conditions, in which a fixed projection of

free surface markers in the xOy plane is implied

$$\frac{\mathrm{d}\eta}{\mathrm{d}t}(\mathbf{M}) = \frac{\partial\phi}{\partial z} - \frac{\partial\phi}{\partial x}\frac{\partial\eta}{\partial x} - \frac{\partial\phi}{\partial y}\frac{\partial\eta}{\partial y}, \quad \mathbf{M}(x,y,\eta,t) \in S_{\mathrm{F}} \tag{28}$$

$$\frac{\mathrm{d}\phi}{\mathrm{d}t}(\mathbf{M}) = -\eta - \frac{1}{2}|\nabla\phi|^2 + \frac{\partial\eta}{\partial t}\frac{\partial\phi}{\partial z}, \quad \mathbf{M}(x,y,\eta,t) \in S_{\mathrm{F}} \tag{29}$$

where η is again the free surface elevation, and z still positive upwards with its origin on the mean position of the free surface. And here $\mathrm{d}/\mathrm{d}t$ stands for the pseudomaterial derivative, following a marker vertically with inhibited horizontal motion.

On fixed material boundaries, no-flux Neumann conditions are applied

$$\frac{\partial\phi}{\partial n}(\mathbf{M}) = 0, \quad \mathbf{M}(x,y,z,t) \in S_{\mathrm{B}} \cup S_{\mathrm{BT}} \tag{30}$$

3.2. Formulation for the non-linear diffraction flow

In this diffraction model, an explicit representation of the incident wave system is supposed to be available. The corresponding fluid velocity derives from the potential $\phi_i(\mathbf{M}(x,y,z,t))$, while the undisturbed incident wave elevation is $\eta_i(x,y,t)$. Then we define the diffraction potential and wave elevation by

$$\phi(\mathbf{M}) = \phi_i(\mathbf{M}) + \phi_d(\mathbf{M}), \quad \mathbf{M}(x,y,z,t) \in D \tag{31}$$

$$\eta(\mathbf{M}) = \eta_i(\mathbf{M}) + \eta_d(\mathbf{M}), \quad \mathbf{M}(x,y,\eta,t) \in S_{\mathrm{F}} \tag{32}$$

After some manipulations, the following boundary-value problem to be solved for (ϕ_d, η_d) is obtained:

$$\Delta\phi_d(\mathbf{M}) = 0, \quad \mathbf{M}(x,y,z,t) \in D \tag{33}$$

with on the free surface $[z = \eta(x,y,t)]$

$$\frac{\mathrm{d}\eta_d}{\mathrm{d}t}(\mathbf{M}) = \frac{\partial\phi_d}{\partial z} - \nabla(\phi_i + \phi_d)\nabla(\eta_i + \eta_d) - \frac{\mathrm{d}\eta_i}{\mathrm{d}t} + \frac{\partial\phi_i}{\partial z} - \nu(R)\eta_d \tag{34}$$

$$\frac{\mathrm{d}\phi_d}{\mathrm{d}t}(\mathbf{M}) = -(\eta_d + \eta_i) - \frac{1}{2}|\nabla\phi_d + \nabla\phi_i|^2 + \frac{\partial(\eta_i + \eta_d)}{\partial t}\frac{\partial\phi_d}{\partial z} - \frac{\partial\phi_i}{\partial t} - \nu(R)\phi_d \tag{35}$$

while the condition at infinity is simply

$$\phi_d(\mathbf{M}) \to 0, \quad \mathbf{M}(x,y,z,t) \in D, \quad R \to \infty \tag{36}$$

In these equations, the terms involving ϕ_i and η_i will be evaluated from the incident wave model. Damping terms involving functions $\nu(R)$ have also been included (R denotes the radial distance from the origin). The role of these terms is to absorb diffracted waves on the outer part of the free surface mesh.

Initial conditions in the domain correspond to the incident wave without perturbation

$$\phi_d(\mathbf{M}) = 0, \quad \mathbf{M}(x,y,z,0) \in D \tag{37}$$

On the body, the no-flux conditions writes

$$\frac{\partial \phi_d}{\partial n}(\mathbf{M}) = -\alpha(t)\frac{\partial \phi_i}{\partial n}(\mathbf{M}), \quad \mathbf{M}(x, y, z, t) \in D \tag{38}$$

in which $\alpha(t)$ is a smooth ramp function varying from 0 to 1 during the beginning of the simulation (typically 1–2 wave periods), for regular wave diffraction problems. For wave packets diffraction, as presented in this paper, the incoming flow field is zero in the vicinity of the body at $t = 0$, so this ramp becomes useless.

It must be emphasized that the boundary-value problem being non-linear, Equations (34) and (35) will be satisfied on the instantaneous free surface position, so that the incident potential ϕ_i may possibly be evaluated above the undisturbed incident wave $z = \eta_i(x, y, t)$. This is possible only if the incident potential has a continuous extension above the incident wave. This is the case for regular non-linear incoming waves described by stream-function theory. For arbitrary incoming waves, the time-domain pseudospectral model described in the following section has the same property, as the potential is described using a set of global basis functions defined throughout the domain.

4. FULLY NON-LINEAR PSEUDOSPECTRAL MODELLING OF INCOMING WAVES

4.1. Introduction

The pseudospectral scheme is a *global* approach, in which the solution is expanded in terms of functions known everywhere in the physical domain. This means that the numerical solution is not based on a discretization of the physical domain, contrary to methods more commonly used in hydrodynamics, such as the BEM or the finite-element method (FEM). The main approximation is thus on the truncation of the functional series. When these functions are orthogonal one with each other (as it is the case in the proposed method), the accuracy grows nearly exponentially with the number of functions used in the expansion; this behaviour is referred to as the 'spectral convergence'. The counterpart of this attractive feature is mainly found in the limitation to simple geometrical domains, such as the rectangular tank we use in the present paper. For a general review of the applications of spectral methods in general CFD, see References [17, 18]. In applications to free surface inviscid flows it is possible to find, for some geometries, orthogonal functions satisfying Laplace's equation, so that the coefficients of the spectral expansion are determined through the free surface conditions only. This approach has first been combined to a perturbation expansion of the free surface conditions [19, 20] and, more recently, it has been used to solve fully non-linear 2D [21, 22] or 3D [23] free surface problems. In the present paper, a pseudospectral approach is applied to generate an incoming wave field about a 3D cylinder structure placed in a 2D rectangular tank, starting from an initial non-flat free surface deformation. The basis functions set for the spectral expansion are the natural modes of the fluid domain, they compose an orthogonal basis and solve the boundary-value problem in the physical space.

4.2. Mathematical formulation

In this section, a two-dimensional tank of mean water depth h and length L_x is under consideration, partially field with an inviscid fluid. A Cartesian fixed co-ordinate system $(O; \mathbf{x}, \mathbf{z})$ is

defined in the same manner as previously, O being situated at the level of water at rest and at the left wall of the tank. We also assume the flow to be irrotational; thus the fluid velocity in the whole fluid domain D derives again from a scalar potential $\phi_i(\mathbf{M}(x,z,t))$ satisfying Laplace's equation

$$\Delta\phi_i(\mathbf{M}) = 0, \quad \mathbf{M}(x,z,t) \in D \tag{39}$$

On the tank walls and bottom the potential ϕ_i has to satisfy homogeneous Neumann conditions. Initially the fluid is at rest. We also suppose the free surface to be single valued and represented at every time by $z = \eta_i(x,t)$. Hence, the non-dimensional kinematic and dynamic conditions at the free surface S_F are formulated as follows (non-dimensionalization being done with respect to the depth h and the acceleration of gravity g):

$$\frac{\partial\eta_i}{\partial t}(\mathbf{M}) = \frac{\partial\phi_i}{\partial z} - \frac{\partial\phi_i}{\partial x}\frac{\partial\eta_i}{\partial x}, \quad \mathbf{M}(x,\eta_i,t) \in S_F \tag{40}$$

$$\frac{\partial\phi_i}{\partial t}(\mathbf{M}) = -\eta_i - \frac{1}{2}\left[\left(\frac{\partial\phi_i}{\partial x}\right)^2 + \left(\frac{\partial\phi_i}{\partial z}\right)^2\right], \quad \mathbf{M}(x,\eta_i,t) \in S_F \tag{41}$$

A set of initial conditions is joined to these equations:

$$\phi_i = 0, \quad \frac{\partial\phi_i}{\partial x} = 0, \quad \frac{\partial\phi_i}{\partial z} = 0, \quad \mathbf{M}(x,z,0) \in D \tag{42}$$

$$\eta_i = \eta_{i_0}(x), \quad \mathbf{M}(x,\eta_i,0) \in S_F \tag{43}$$

where the initial water elevation η_0 is such that the mean water elevation is null at $t = 0$.

We further decompose the velocity potential ϕ_i into a truncated series of the natural modes of the tank

$$\phi_i(\mathbf{M}) = \sum_{m=0}^{N_\phi} a_m(t)\psi_m(x,z), \quad \mathbf{M}(x,z,t) \in D \tag{44}$$

where the spatial functions $(\psi_m(x,z), m = 0 \to N_\phi)$ are the natural modes of the tank, and the $(a_m(t), m = 0 \to N_\phi)$ the 'modal time amplitudes'. Having introduced this decomposition into the governing equation (39) and homogeneous Neumann conditions on the tank walls it comes

$$\psi_m(x,z) = \cos(k_m x)\frac{\cosh[k_m(z+1)]}{\cosh[k_m]} \tag{45}$$

in which $k_m = m\pi/L_x$ is the wave number associated to the mth mode.

Now, the only remaining unknowns of the problem are the modal time amplitudes $a_m(t)$ and the free surface elevation η_i, which have to satisfy the free surface conditions rewritten as

$$\frac{\partial\eta_i}{\partial t}(\mathbf{M}) = \frac{\partial\phi_i}{\partial z} - \frac{\partial\phi_i}{\partial x}\frac{\partial\eta_i}{\partial x}, \quad \mathbf{M}(x,\eta_i,t) \in S_F \tag{46}$$

$$\sum_{m=0}^{N_\phi} (a_m)_t(t)\ \cos(k_m x)\frac{\cosh[k_m(\eta_i+1)]}{\cosh[k_m]} = -\eta_i - \frac{1}{2}|\nabla\phi_i|^2, \quad \mathbf{M}(x,\eta_i,t) \in S_F \tag{47}$$

4.3. Numerical solution

These last two equations (46) and (47) are discretized at N_η different collocation nodes of the free surface S_F, with $N_\eta \geqslant N_\phi + 1$. We therefore get N_η and $N_\phi + 1$ unknown values for η^j and a_m, respectively, at each timestep. To update these unknowns, we use the fourth-order Runge–Kutta scheme; knowing the η^j and the a_m at t, this time-marching scheme directly provides the η^j at $t + \Delta t$ from the kinematic free surface condition (46). However, the knowledge of the a_m-unknowns at $t + \Delta t$ requires the additive resolution of an $N_\eta \times (N_\phi + 1)$ linear system assembled from the dynamic condition (47) taken at the N_η collocation nodes. This resolution furnishes the N_η $(a_m)_t$ necessary to obtain the a_m-unknowns at each substep of the Runge–Kutta scheme. The previous linear system is either square (if $N_\eta = N_\phi + 1$), or overdetermined (if $N_\eta > N_\phi + 1$). If the system is square, its solution is obtained by means of the preconditioned iterative GMRES solver, whose number of operations is typically $O(N_\eta^2)$ when the number of iterations is small compared to N_η. Otherwise the Householder method for overdetermined systems is chosen; its number of operations being $O(N_\eta^3)$. Overdetermination is applied in some simulations to increase the stability of our solution and help global convergence. This technique was previously used by Kim *et al.* [21]. Numerical results for two- and three-dimensional free surface flows in tanks submitted to forced motions obtained using this formulation were compared to existing data and presented in the recent past, see Reference [23].

5. COUPLING 2D PSEUDOSPECTRAL AND 3D BEM SOLUTIONS

5.1. Coupling aspects

As briefly stated in Section 3.2, the key point of the coupling method proposed in the present work lies in the possibility to estimate the incident wave field potential not only on the undisturbed incident free surface, but also at the instantaneous free surface location. This section is intended to provide arguments supporting the validity of the coupling scheme, as well as to highlight its significant advantages in terms of numerical efficiency, compared to a direct approach of the non-linear wave–body interaction problem.

The most simple way to get convinced of the validity of the global quantities decomposition, as proposed in Equations (31) and (32), is to consider it as a purely mathematical change of variables, in which the new unknowns (the scattered parts) derive from the previous ones (the total free surface deformation and velocity potential) by a simple subtraction of known parts (the incident ones). This change of variables implies no approximation, as we keep on solving the original fully non-linear problem, through equations (33)–(38). Especially, fully non-linear free surface conditions (34) and (35) remain applied at the instantaneous free surface location. However, for this change of variables to be possible, the incident velocity field must possess a continuation across the incident free surface, so that it can always be evaluated, even when the instantaneous total free surface lies *above* the incident one. This condition is satisfied both by the stream-function theory we use to model regular non-linear waves, and by the 2D pseudospectral scheme introduced in this paper to generate non-linear irregular wave fields, as in both schemes the potential is expressed in the form of series of harmonic functions defined continuously in the whole domain. On the contrary, such a scheme could not be applied with incident waves produced

by a 2D fully non-linear BEM code, for instance, because the last condition would not be fulfilled.

The motivation for applying this coupling method is to be found in its computational efficiency. First, the incident wave field is described either semi-analytically in the case of regular waves, or with quasi-arbitrary accuracy for 2D irregular waves, using the proposed pseudospectral method. The incident wave field is therefore not affected by discretization errors in the 3D numerical scheme used to model diffracted quantities. For example, in the present illustration of the coupling scheme, the size of the free surface mesh and the discretization parameters are only adapted to the diffracted flow, that reduces to outgoing waves in the far field. For a given accuracy, the size of the problem to be solved is then dramatically lowered, compared to a direct approach in which the total 3D flow would have to be simulated. Another important consequence of the change of variable is that conditions at infinity reduce to Equation (36), which simply expresses that the diffracted flow vanishes there. In the numerical scheme this condition is easily accounted for, by absorbing diffracted quantities, through terms added to the free surface conditions in the outer part of the mesh. Consequently, the coupling scheme provides a simple and efficient way to model fully non-linear wave–body interaction problems in an unbounded domain.

Practically, the 3D BEM diffraction code requires the knowledge of the incoming velocity potential ϕ_i, and its derivatives $\partial\phi_i/\partial x$, $\partial\phi_i/\partial z$ and $\partial\phi_i/\partial t$ on the instantaneous position of the free surface, thus possibly *above* the undisturbed incoming free surface as explained previously. The diffraction code needs also to be provided with the incoming free surface elevation η_i and its derivatives $\partial\eta_i/\partial x$ and $\partial\eta_i/\partial t$.

Having stored the modal time amplitudes a_m and their time derivatives $(a_m)_t$ at the corresponding non-dimensional time, the incoming velocity potential ϕ_i and its derivatives may be straightforwardly reconstructed from expressions such as (44) and (45); and this, at any necessary spatial position. On the other hand, the incoming free surface elevation η_i and its spatial derivative $\partial\eta_i/\partial x$ are stored at the collocation nodes and are interpolated in between by means of B-splines. Eventually, the time derivative $\partial\eta_i/\partial t$ is directly derived from all those quantities through the kinematic free surface condition (46).

5.2. *Generation of a wave packet using a non-flat initial free surface deformation*

In order to check the effectiveness of the coupling of our 2D pseudospectral and 3D BEM models, we have proceeded to the simulation of a 2D wave packet interacting with a bottom-mounted cylinder. The wave packet is generated by means of a simple non-flat initial deformation imposed to the free surface at $t=0$, the fluid kinematics being set null. The incoming wave packet thus results of the numerical solution of a 2D fully non-linear Cauchy–Poisson problem.

5.2.1. Data set. In our case, the initial Cauchy–Poisson 'bump' is located at the left-side wall of the 2D 80×1-rectangular wave tank used in our 2D pseudospectral model. Resulting waves will propagate from left to right, and disperse all along the tank during the simulation. The initial non-flat free surface deformation η_{i_0} is chosen as such

$$\begin{aligned} &\eta_{i_0}(x)=\beta(\mathrm{e}^{-x^2}-\mathrm{e}^{-16})-k_\beta\left(1+\cos\left(\frac{\pi x}{4}\right)\right) && \text{for } 0\leqslant x\leqslant 4\\ &\eta_{i_0}(x)=0 && \text{for } x>4 \end{aligned} \tag{48}$$

where β is an amplitude coefficient and k_β the corresponding coefficient ensuring the nullity of the initial volume (compared to the volume of water at rest), the co-ordinates origin being chosen on the left wall at the level of water at rest. The number of natural modes selected for our converged simulations is $N_\phi+1=301$, and the number of collocation nodes chosen is $N_\eta=601$. That is to say we use a 2-times overdetermination which ensures the stability of our solution even for the highest steepness used in the simulations.

Concerning the BEM model parameters now, the 3D BEM mesh is axisymmetrical, composed of three different surfaces: the vertical bottom-mounted cylindrical body itself of radius $r_{\text{body}}/h=0.5$, a free-surface ring-shaped mesh refined close to the body, and an outer vertical cylinder of radius $r_{\text{outlet}}/h=8$. The co-ordinates origin is situated at the cylinders' centre, at the vertical level of water at rest. On the free surface, a ring-shaped absorbing zone goes from $r/h=4.5$ to the outer cylinder. The 3D mesh selected counts 11 600 panels. The fluid is at rest at $t=0$, and the free surface is undisturbed.

The matching between the 2D and 3D domains is done considering the 3D origin to have the following co-ordinates in the 2D domain: $(x/h=10, z/h=0)$. The time step used in the pseudospectral code is chosen as one half of the one used for BEM computations, this in order to provide incident wave information at each step of the diffraction code time-marching scheme without interpolation.

5.2.2. Results. Two 2D pseudospectral/3D BEM-coupled simulations were run, further referred as '4%-steepness' and '6%-steepness' cases. The steepness is defined here as the maximum—in time and at the cylinder position $(x/h=10)$—of the ratio $(C+T)/\lambda$, where C and T stand for the heights of two successive crest and trough, and where λ is two times the x-distance between this crest and this trough. The time steps used in the pseudospectral code are $\Delta t=2.62\times10^{-2}$ and 1.31×10^{-2} for the '4%-steepness' and '6%-steepness' cases, respectively.

Figures 5 and 6 show the time evolution of the incoming free surface in the two cases, the cylinder being placed quite close to the initial hump (at $x/h=10$). In Figure 5, the incoming free surface deformation is plotted at four different times of the dispersion of the wave packet, and in Figure 6 one can see the time series of the incoming water elevation at the cylinder location. At $t=0$, the free surface is deformed only close to the left-side wall of the 2D tank (Equation (48)), the cylinder is therefore surrounded by still water. Then the development of a wave train clearly appears, long waves first followed by shorter and shorter waves. This is a classical figure of dispersion, group velocities increasing with wavelengths. The packet presents also a typical non-linear behaviour with higher crests than troughs, which is very logically more pronounced for the highest steepness. After a long enough period of time, the water is back to rest in the vicinity of the cylinder location.

In Figure 7, we present the runups on the vertical cylinder; the incoming, scattered and total water elevation at the upwave and downwave positions on the cylinder waterline are plotted. At this location, the relative amplitude of the scattered wave compared to the total elevation is noticeable (close to 1 in the 6%-steepness case); and its average phase is as such that total crests and troughs are magnified. The irregular pattern of the packet generated is clearly visible as well: wave heights and wave periods are distributed in the ranges $[0.,0.24]$ and $[1.,7.]$, respectively, corresponding range in wavelengths being at square of the one in periods.

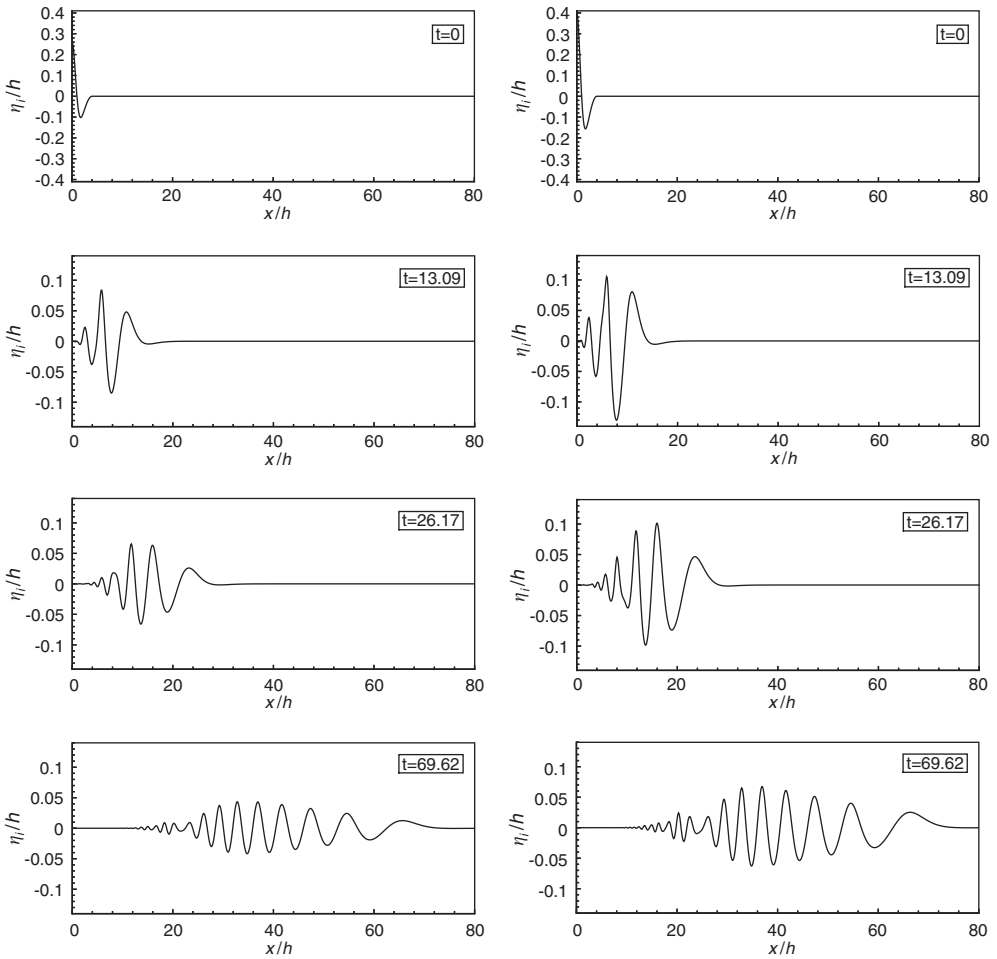

Figure 5. Incoming wave elevation in the tank at four different times (on the left: 4% steepness, on the right: 6% steepness).

In Figure 8, we give 3D snapshots of the fluid domain for three different times of the '6%-steepness' case. The wave packet propagates from left to right. The first plot on top of the figure shows the beginning of the interaction phase, the free surface deformation is mostly two-dimensional up to that time. The second plot corresponds to the highest wave in the packet impinging on the cylinder inducing strong diffraction effects, that propagate radially from the cylinder. On the last plot, the main part of the incident wave packet has propagated away, leaving the diffraction pattern around the cylinder clearly visible.

Hence, the coupling of our two models proved to be effective and stable, reproducing well the fully non-linear diffraction of the wave packet on the cylinder. Moreover, it has been checked that the 2D pseudospectral model actually presents the expected characteristics in terms of convergence and accuracy. In the simulations relative error on the volume and energies was of the order of 10^{-7}, ensuring a very accurate description of the incoming wave field in the 3D BEM model.

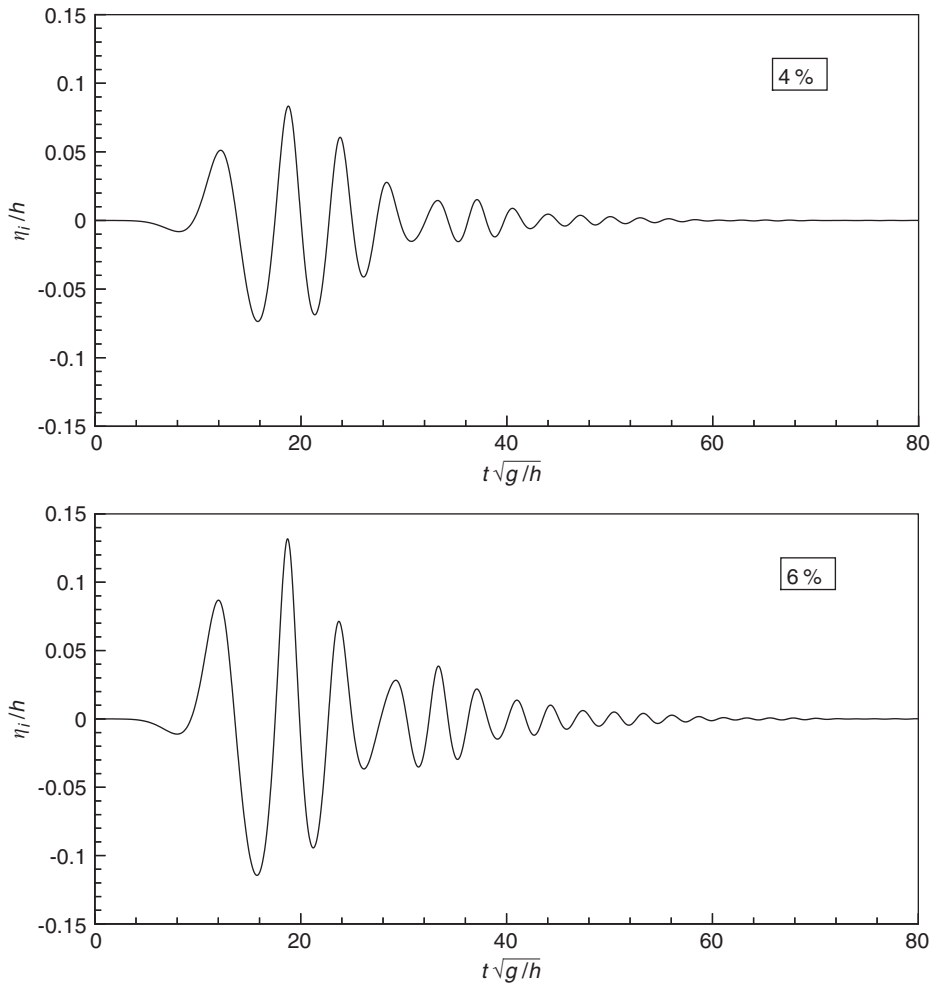

Figure 6. Time series of the incoming wave elevation at the cylinder location for two steepness.

6. CONCLUSION

A second-order and a fully non-linear time-domain approaches for water wave diffraction by arbitrary 3D structures have been presented in this paper. In both models, a BEM solution of the initial boundary-value problem is implemented. The BEM is based on piecewise linear isoparametric triangular elements, while higher-order local interpolation using spline patches is applied for the computation of fluid velocities and free surface geometry. This mixed scheme combines a very good computational efficiency, compared to higher-order BEMs, with a satisfactory accuracy. In second-order simulations, the usefulness of the scheme is demonstrated by simulating the diffraction of bichromatic waves by vertical cylinders over a large period of time, with excellent stability of the computed wave field. These results open the way to the long time simulation of the interaction of irregular short-crested seas with offshore

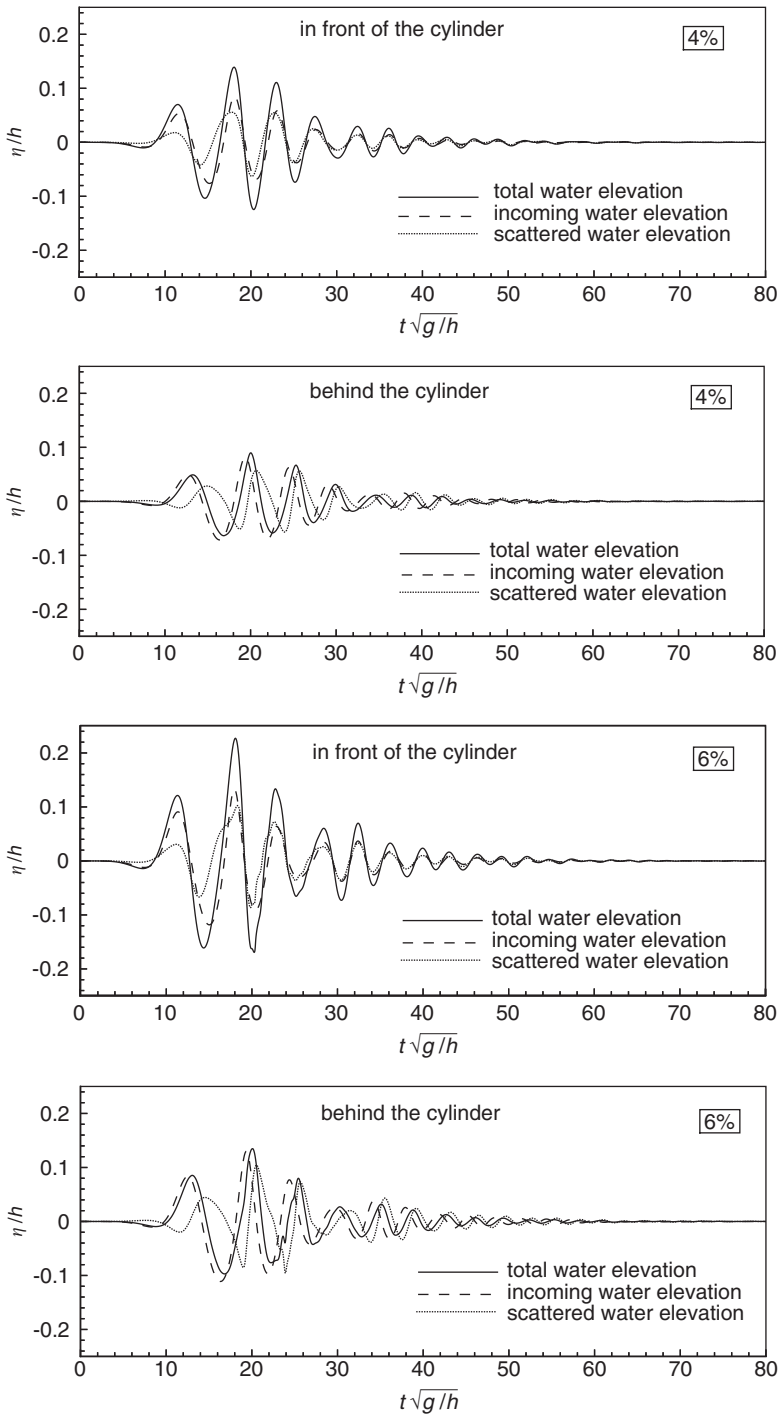

Figure 7. Time series of incoming, scattered and total wave elevation in front and behind the cylinder, for two steepness.

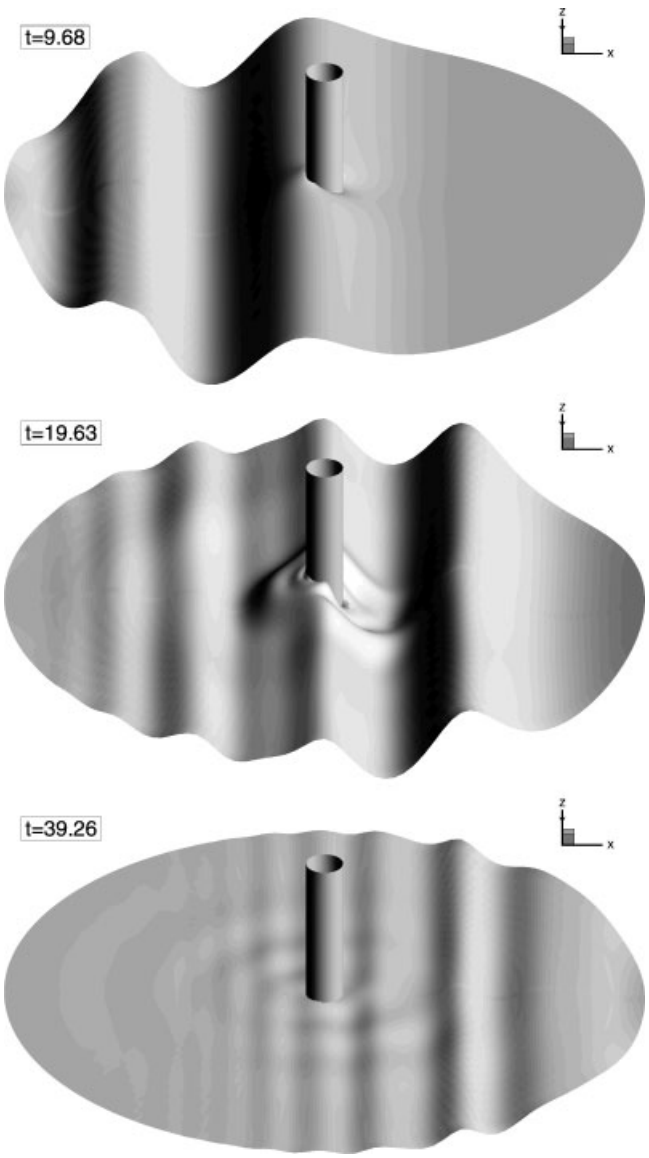

Figure 8. 3D view of the free surface; '6%-steepness' case. Vertical magnification = 10.

structures. In this way, a direct time-domain estimation of the statistics of second-order loads, runup and airgap will be possible.

The same boundary-value solver is used in fully non-linear simulations, combined with an original formulation for the non-linear diffraction problem. One of the advantages of this formulation is that incident and diffracted waves may be represented using different approaches. For instance, a 2D scheme may be used to provide an accurate representation of incoming waves, at a negligible cost with respect to that of the 3D model used to simulate the diffraction

of this incident wave. In addition, the perturbations represented by (ϕ_d, η_d) are composed of waves propagating in radial directions, allowing relatively coarse meshes to be adopted far from the body, in the absorbing zone. This results in considerable savings of memory and CPU time, without loss of accuracy. On the other hand, this formulation is not universal and relies on the availability of an explicit model for the incident wave, with appropriate continuity properties across the incident wave profile. Initially developed with regular incident waves represented by a stream-function model, the formulation has been extended in this paper to more general irregular incoming waves, by coupling the 3D BEM diffraction code with a 2D fully non-linear pseudospectral formulation for unsteady inviscid free surface flows. The effectiveness of this coupling is demonstrated by simulating the diffraction of 2D wave packets of increasing steepness with a vertical bottom-mounted cylinder. In the near future, the pseudospectral solver will be improved in order to simulate the generation of waves by a physical wave maker. Other developments include the modelling of short-crested wave systems using the pseudospectral approach, and their interaction with structures.

REFERENCES

1. Molin B. Second-order diffraction loads upon three-dimensional bodies. *Applied Ocean Research* 1979; **1**: 197–202.
2. Chau FP, Eatock-Taylor R. Second-order wave diffraction by a vertical cylinder. *Journal of Fluid Mechanics* 1992; **240**:571–579.
3. Kim Y, Kring DC, Sclavounos PD. Linear and nonlinear interaction of surface waves with bodies by a three-dimensional panel method. *Applied Ocean Research* 1997; **19**:235–249.
4. Büchmann B, Skourup J, Cheung KF. Run-up on a structure due to second-order waves and a current. *Applied Ocean Research* 1998; **20**(5):297–308.
5. Ferrant P, Pelletier K. Second-order wave diffraction patterns about complex offshore structures. *Proceedings of the 10th International Offshore and Polar Engineering Conference*, *Seattle*, vol. 3, 2000; 686–693.
6. Celebi MS, Kim MH, Beck RF. Fully nonlinear 3D numerical wave tank simulation. *Journal of Ship Research* 1998; **42**(1):33–45.
7. Ferrant P. Simulation of strongly nonlinear wave generation and wave–body interaction using a 3D MEL model. *Proceedings of 21st ONR Symposium on Naval Hydrodynamics*, *Trondheim*, 1996; 93–108.
8. Rienecker MM, Fenton JD. A Fourier approximation for steady water waves. *Journal of Fluid Mechanics* 1981; **104**:119–137.
9. Ferrant P, Molin B, Malenica Š. Nonlinear wave loads and runup on a vertical cylinder. In *Nonlinear Water Wave Interaction*, Mahrenholtz O, Markiewicz M (eds). WIT Press: Southampton, 1999; 101–135.
10. Ferrant P. Run-up on a cylinder due to waves and a current: potential flow solution with fully nonlinear boundary conditions. *International Journal of Offshore and Polar Engineering* 2001; **11**(1):33–41.
11. Büchmann B, Ferrant P, Skourup J. Run-up on a body in waves and current. Fully nonlinear and finite order calculations. *Applied Ocean Research* 2000; **22**:349–360.
12. Dalzell JF. A note on finite depth second-order wave-wave interactions. *Applied Ocean Research* 1999; **21**: 105–111.
13. Le Méhauté A. In Interpolation et approximation par des fonctions polynômiales par morceaux dans R^n. *Ph.D. Thesis*, Université de Rennes I, France, 1984 (in French).
14. MacCamy RC, Fuchs DV. In Waves forces on piles: a diffraction theory. *Tech. Mem.*, vol. 69, US Army Coastal Engineering Research Center, 1954.
15. Linton CM, Evans DV. The interaction of waves with an array of vertical circular cylinders. *Journal of Fluid Mechanics* 1990; **215**:549–569.
16. Nielsen FG. Comparative study of airgap under floating platform and runup on platform columns. *Preliminary Report for ISSC*, 2000.
17. Hussaini MY, Zang TA. Spectral methods in fluid dynamics. *Annual Review of Fluid Mechanics* 1987; **19**: 339–367.
18. Fornberg B. In *A Practical Guide to Pseudospectral Methods*. Cambridge University Press: Cambridge, MA, 1995.
19. Fenton JD, Rienecker MM. A Fourier method for solving nonlinear water-wave problems: application to solitary-wave interactions. *Journal of Fluid Mechanics* 1981; **118**:441–443.

20. Dommermuth DG, Yue DKP. A high-order spectral method for the study of nonlinear gravity waves. *Journal of Fluid Mechanics* 1987; **184**:267–288.
21. Kim MJ, Moon HT, Lee YB, Choi SK, Kim YK, Nam HY, Cho M. A spectral method for free surface flows of inviscid fluids. *International Journal for Numerical Methods in Fluids* 1998; **28**:267–288.
22. Chern MJ, Borthwick AGL, Eatock-Taylor R. A pseudospectral σ-transformation model of 2-D nonlinear waves. *Journal of Fluids and Structures* 1999; **13**:607–630.
23. Ferrant P, Le Touzé D. Simulation of sloshing waves in a 3D tank based on a pseudospectral method. *Proceedings of the 16th Workshop on Water Waves and Floating Bodies*, 2001.

